

The STAGGER-grid: A grid of 3D stellar atmosphere models

VI. Surface appearance of stellar granulation

Z. Magic^{1,2} and M. Asplund²

¹ Max-Planck-Institut für Astrophysik, Karl-Schwarzschild-Str. 1, 85741 Garching, Germany
e-mail: magic@mpa-garching.mpg.de

² Research School of Astronomy & Astrophysics, Cotter Road, Weston ACT 2611, Australia

Received ...; Accepted...

ABSTRACT

Context. In the surface layers of late-type stars, stellar convection is manifested with its typical granulation pattern due to the presence of convective motions. The resulting photospheric up- and downflows leave imprints in the observed spectral line profiles.

Aims. We perform a careful statistical analysis of stellar granulation and its properties for different stellar parameters.

Methods. We employ realistic 3D radiative hydrodynamic (RHD) simulations of surface convection from the STAGGER-grid, a comprehensive grid of atmosphere models that covers a large parameter space in terms of T_{eff} , $\log g$, and $[\text{Fe}/\text{H}]$. Individual granules are detected from the (bolometric) intensity maps at disk center with an efficient granulation pattern recognition algorithm. From these we derive their respective properties: diameter, fractal dimension (area-perimeter relation), geometry, topology, variation of intensity, temperature, density and velocity with granule size. Also, the correlation of the physical properties at the optical surface are studied.

Results. We find in all of our 3D RHD simulations stellar granulation patterns imprinted, which are qualitatively similar to the solar case, despite the large differences in stellar parameters. The granules exhibit a large range in size, which can be divided into two groups – smaller and larger granules – by the mean granule size. These are distinct in their properties: smaller granules are regular shaped and dimmer, while the larger ones are increasingly irregular and more complex in their shapes and distribution in intensity contrast. This is reflected in their fractal dimensions, which is close to unity for the smaller granules, and close to two for larger granules, which is due to the fragmentation of granules.

Conclusions. Stellar surface convection seems to operate scale-invariant over a large range in stellar parameters, which translates into a self-similar stellar granulation pattern.

Key words. convection – hydrodynamics – radiative transfer – stars: atmospheres – stars: general – stars: late-type – stars: solar-type

1. Introduction

In the envelopes of cool stars, the energy resulting from the nuclear burning at the center is transported through convective energy transport, which involves the ascension of hot, buoyant plasma towards the surface. At the optical surface, the overturning convective motions into downdrafts do not come to rest immediately, instead the upflows overshoot well into the visible photosphere due to its inertia, hence leaving an imprint in the emergent radiation in form of a typical granulation pattern. The visible stellar surface of late-stars is patterned with bright elements (granules) interspersed by the dark intergranular lane. Understanding convection is an important aspect for the energy transport in late-type stars, however, this is a non-trivial task due to the non-linear and non-local nature of (turbulent) surface convection.

The Sun shows a distinct granulation pattern on its observable (optical) surface, which is the manifestation of convection that transports energy to the surface. The solar granulation pattern has been subject to manifold observational studies over the last decades with progressively increasing resolution due to technological advances (e.g. Roudier & Muller 1986; Hirzberger et al. 1997, 1999a,b; Schrijver et al. 1997; Bovelet & Wiehr 2007, 2001; Abramenko et al. 2012). Nowadays high-resolution

solar observations are comparable to the typical numerical resolution with a few tens of kilometers. The observational developments were accompanied by improvements in the detection and derivation of statistical properties of solar granulation. Moreover, details of the solar small-scale magnetic structures has also been studied (Solanki 1993; Janßen et al. 2003; Carlsson et al. 2004; Abramenko & Longcope 2005; Stein & Nordlund 2006; Wiehr & Bovelet 2009).

Until the advent of realistic 3D radiative hydrodynamic (RHD) simulations, which involves the (computationally expensive) solution of the hydrodynamic equations coupled with a realistic radiative transfer (Nordlund 1982; Steffen et al. 1989), direct comparisons of theoretical predications with the solar granulation properties were absent. In contrast to theoretical 1D models, such 3D models are capable of predicting the typical stellar granulation pattern imprinted in the (bolometric) intensity map emerging from the stellar surface. They have revealed that stellar surface convection is driven by the large-amplitude entropy fluctuations in a thin optical surface boundary layer, where the energy can escape into space (see Stein & Nordlund 1998; Nordlund et al. 2009). The dark intergranular lanes stem from the entropy-deficient plasma that descends into narrow turbulent downdrafts, while the granules are warm upflowing plasma. These flows exhibit a distinct asymmetry in its thermodynamic properties, leading to inhomogeneities and velocities, which has

Send offprint requests to: magic@mpa-garching.mpg.de

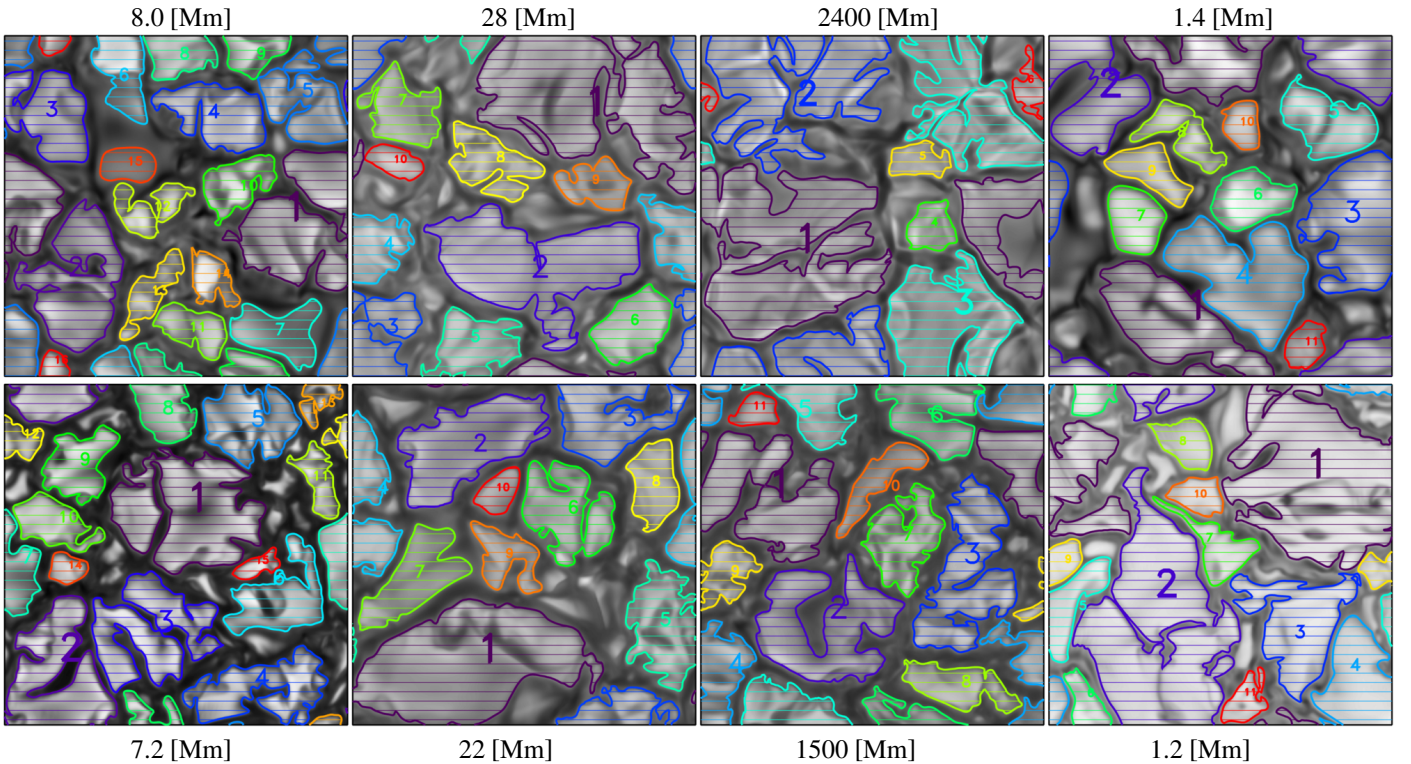


Fig. 1: Emergent (bolometric) intensity map (*gray contours*) over-plotted with the colored-coded contours of the recognized granules with solar (*top panel*) and $[\text{Fe}/\text{H}] = -3.0$ (*bottom*). From *left to right*: the Sun ($T_{\text{eff}}/\log g = 5777\text{K}/4.44$), turnoff star (6500K, 4.0), K-giant (4500K, 2.0) and K-dwarf (4500K, 5.0). The granules are numbered in order of decreasing granule size at its respective barycenter (large characters refers to large granule size).

been compared with observations of the Sun (e.g., Asplund et al. 2000, 2004; Carlsson et al. 2004; Pereira et al. 2009b,a, 2013) and other stars (e.g., Nordlund & Dravins 1990; Collet et al. 2006, 2007; Ramírez et al. 2008, 2009, 2010; Chiavassa et al. 2009, 2010, 2011, 2012). These comparisons have confirmed the realism of the 3D RHD simulations. Due to the increasing computational power, various grids of 3D RHD atmosphere models have been constructed, in order to study surface convection. The `CFIST`-grid employing the `co5BOLD`-code, studied the impact of granulation (see Ludwig et al. 2009; Freytag et al. 2012; Kučinskas et al. 2013; Tremblay et al. 2013). Trampedach et al. (2013) established a grid of 3D RHD models with solar metallicity. Also, efforts are being made with the `MURAM`-code (see Vögler & Schüssler 2003; Beeck et al. 2013a,b). We have computed the `STAGGER`-grid, a grid of 3D RHD model atmospheres (Magic et al. 2013a,b, hereafter Paper I and II), and used our 3D models for several applications (Magic et al. 2014b,a, hereafter Paper III and IV).

In the present work, we perform an extensive analysis of the stellar granulation properties based on the `STAGGER`-grid. We want to address the following key question: How do the stellar granulation properties change for different stellar parameters? First, we explain the granule recognition method that we have used to detect the individual granules from the (bolometric) intensity maps of the 3D simulations (Sect. 2). Then, we discuss successively the various properties of individual granules, such as their diameter (Sect. 3), the fractal dimension (Sect. 4), the geometry (Sects. 5), the variation of the intensity, temperature, density, velocity with granule size (Sect. 6), and finally the properties at the optical surface (Sect. 7).

2. The granule recognition method

2.1. Detection from intensity maps

Several methods for detecting granules in observed solar images have been developed over the years. Classically, a single-level clip of an intensity image is used for the granule recognition, where the small and large features are filtered out by spatial pass-band Fourier filtering. These "Fourier-based recognition" techniques have been the most commonly applied ones in the past, and are fast, but also inaccurate (see Roudier & Muller 1986; Hirzberger et al. 1997). Another possible approach is to trace granules with a single fixed relative intensity-level, e.g., between 0.97 and 1.03, as proposed by Abramenko et al. (2012). However, in this work we prefer the more robust "multiple level tracking" algorithm that was developed by Bovelet & Wiehr (2001). It is a simple, yet very powerful tool to extract the granules from the (bolometric) intensity map alone. The basic idea behind this method is to find (granular) shapes repeatedly for decreasing intensity level clips, thereby increasing their filling factors, until a predefined threshold filling factor is matched. One obtains unambiguously the granules with a single input parameter being the filling factor for the upflows, f_{up} . Since the latter is basically the same for all stellar parameters with $f_{\text{up}} \approx 2/3$ (see Paper I), the granule-recognition is performant with the multiple level tracking algorithm. Furthermore, we find this algorithm being very fast, robust, and works for all stellar parameters. To demonstrate this, we show the results for the Sun, a turnoff star, a K-giant, and a K-dwarf as well as their metal-poor ($[\text{Fe}/\text{H}] = -3$) analogs in Fig. 1.

Following the multiple level tracking algorithm, we traced the granules in our simulations and computed the respective fill-

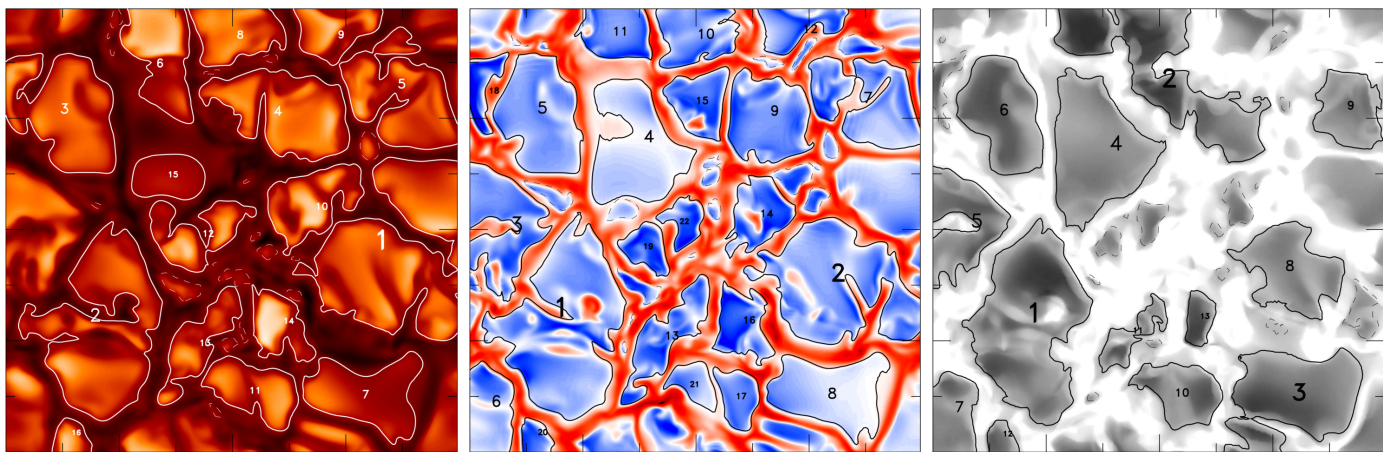


Fig. 2: Comparison of the solar granules detected from different variables. *Left figure*: the visible (bolometric) intensity map (orange contour); *middle figure*: the averaged vertical velocity (Eq. 1; up/down: blue/red); and *right figure*: the integrated temperature excess (Eq. 2; gray contour).

ing factor, f_i , of the considered intensity-level. We started at the relative intensity $\bar{I} = 1.2$ and decreased the intensity level down to 0.97 in steps of 0.01 until the threshold with $f_{\text{up}} = 0.60$ was reached for all stellar parameters. We chose the threshold value being slightly lower than the average filling factor ($f_{\text{up}} \approx 2/3$), in favor of a cleaner separation between the granules. We enlarged the intensity maps by exploiting their horizontal periodicity, and determined the area and equivalent diameters, as well as further properties for each granule. We dismissed very small patches and matched the fragmented parts of granules that were located at the edge. We classified them in two populations: small (fractional) granules and large granules with the latter being larger than the average area. Furthermore, we singled out dark spots and bright points located within larger granules. Following Abramenko et al. (2010) we enhanced the contrast of the intensity by subtracting the values \hat{I} smoothed by a boxcar average with window size of 5 pixels, and computed the root-mean-square (RMS) for $I_{\text{rms}} = I - \hat{I}$. Then, the bright points were detected at the 2σ -threshold relative to the other granules. We performed the granule-recognition for each stored snapshot of the time-series, thereby leading to large sample of granules for an individual simulation (e.g., Sun ~ 3800 for 150 snapshots every 30 s).

2.2. Detection from vertical velocity and temperature

Besides the intensity map, we also detected granules from the vertical velocity and the temperature excess with the multiple-level-tracking algorithm. The emergent (bolometric) intensity is computed for disk-center, therefore, it is a 2D representation of the 3D granulation structure present in the superadiabatic region of the convection zone. To account for the depth-dependence of the coherent granulation structures, we averaged the vertical velocity and integrated the temperature excess as well.

We averaged the vertical velocity on layers of constant Rosseland optical depth from the optical surface to the peak (maximum) of the superadiabatic gradient (the granulation can be found in these layers best) over ten equidistant layers in steps of $\Delta \log \tau_{\text{Ross}} = 0.1$, i.e.

$$\tilde{v}_z(x, y) = \frac{1}{10} \sum_{i=1}^{10} v_z(x, y, z_i). \quad (1)$$

The granules are determined on the zero velocity contour of $\tilde{v}_z(x, y)$. The averaged vertical velocity is independent of any input parameter, however, it relies on the assumption that the coherent granular structures are given in the superadiabatic region. One could also use the vertical velocity present at the optical surface, however, then one would neglect the depth-dependence, while our approach by averaging over several layers does.

We computed the temperature fluctuations for each layers by normalizing it with the horizontal average, i.e. $\delta T_z = \Delta T_z / \langle T \rangle_z$. Then, we determined the temperature excess, $\delta T = \delta T > \max(\langle \delta T \rangle_z) / 5$, which are the (positive) temperature fluctuations above the threshold of one-fifth of the maximum mean horizontal temperature fluctuations. The relative threshold allows the method to work for different stellar parameters. We integrated the temperature fluctuations from just above the optical surface to the bottom of the simulation box with

$$\Theta(x, y) = \int_{\langle \tau \rangle = 0.1}^{\text{bot}} \delta T(z) dz. \quad (2)$$

The granules are retrieved with the clip-level of the unity (average) contour of $\Theta(x, z)$. In contrast to the intensity map, this method is independent of any assumption on the filling factor. We remark that the temperature excess, δT , is a convenient quantity to illustrate the topology of the superadiabatic convective cells (under-dense regions with heat-excess).

In Fig. 2, we compare the detected granules from a solar simulation snapshot with the three methods. Since the underlying variables exhibit distinct features, the recognized granules differ slightly, in particular, the boundaries between close granules is interpreted differently. Nonetheless, one can clearly see that the granules correlate with bright upflowing regions of significant T -excess.

The above mentioned granule detection methods assume that bright regions in the intensity maps associate with the hotter and lighter stellar plasma leading to the upflowing granules, which is normally fulfilled, as we demonstrate in Sect. 7.2. The remaining dark regions in the intensity maps inherently consist of cool, dense gas, which one usually refers as the (negatively buoyant) downdrafts.

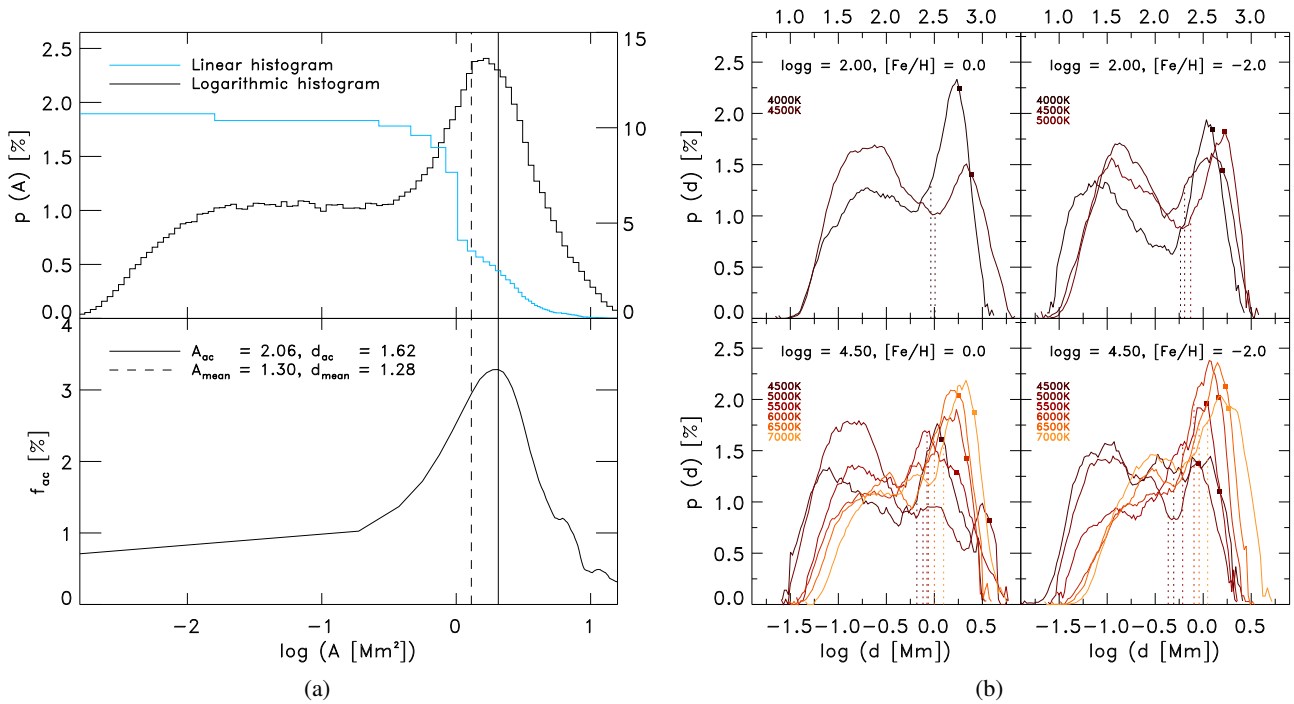


Fig. 3: *Left figure*: The linear and logarithmic histogram of the granule area, A , (*top panel*; *blue and black line*, respectively) and the area contribution, f_{ac} , (*bottom*) derived from our solar simulation. The bin sizes for the histograms are 0.186 Mm and 0.041 dex. We indicated the location of the mean granule area averaged over all granules (*dashed*) and the maximum of f_{ac} (*solid line*). *Right figure*: The logarithmic histograms of the granule size, d_{gran} , smoothed with a moving-average over 10 elements. Furthermore, we indicated the mean granule diameters (*dotted lines*, see Fig. 4) and the dominant scales, d_{ac} (*filled squares*). Note the difference in abscissa between the top and bottom panel.

3. Diameter of granules

From the area of the granules we determined the equivalent diameter with $d_{gran} = 2\sqrt{A_{gran}/\pi}$, which is the diameter of a circle that has the same area A_{gran} . With the granule size we refer to d_{gran} or A_{gran} in the following. Furthermore, we determined the unique barycenter, $\mathbf{x}_{bc} = \sum \mathbf{x}_i A_i / A_{gran}$, where the summation runs over all pixels enclosed by the contour of the granule, and \mathbf{x}_i is the vector pointing to the cell i , and A_i is the pixel area. The granule size is the first property we want to address, therefore, we show the histogram of the granule areas of the Sun in Fig. 3a. The range in granule sizes is very large (typically spanning four orders of magnitude), therefore, a histogram considering a linear equidistant granule size for the histogram bins would overestimate the smallest values by employing very large steps (see Fig. 3a). This would result in a bottom-heavy distribution and the misleading conclusion of a dominant large number of small granules (see Roudier & Muller 1986; Hirzberger et al. 1997; Abramenko et al. 2012). Therefore, we advise against a linear binning of the histograms for starkly varying quantities like the granule size, and instead consider logarithmic granule area for the histograms. In Fig. 3a the histogram exhibits a maximum close to the mean granule size, which we refer to as the mode of granule size, i.e. $d_h = \max[p(A)]$. The distribution around the mode of the granule size is very asymmetric with a long tail towards smaller size. These two regimes (separated by d_h) represent on the one hand the oversized fragmenting granules and the other hand the resulting fragments. The (fragmented) small-scale granules were found in high-resolution solar observations by Abramenko et al. (2012). The fragmentation of granules is a

continuous process, therefore, the distribution of granule sizes is also continuous, and it covers a fairly large range.

Another possibility to quantify the granule size distribution is the area contribution function, which is given by $f_{ac} = n_i A_i / A_{tot}$, with n_i being the number of elements within the area bin A_i , and $A_{tot} = \sum n_i A_i$ being the total area of all granules. The area contribution function is in principle a histogram of granule size, which is weighted with the contribution of area to the total area (Roudier & Muller 1986). We noted above that a linear granule size is overestimating the histogram for smaller granules. The contribution function has the intrinsic advantage that a large number of small granules contributes only little to f_{ac} , since their area is small. It depicts the dominant granule size, which contributes most to the radiation (radiative losses occur mostly from granules, which are hotter and have a larger area), independently of the linear or logarithmic bin sizes. In Fig. 3a we show the area contribution function resulting from the solar simulation. We also label the dominant granule size with the maximum, i.e. $d_{ac} = \max[f_{ac}]$, which leads to the further definition $A_{ac} = \pi(d_{ac}/2)^2$. Similar to the above finding with the mode d_h , the dominant granule size divides the distribution into two regimes at a very similar value, which further supports the location of the "typical" granule size. The decline towards larger granule sizes is similar, but the lower part is noticeably smaller than the histogram (both are not expected to coincide entirely due to their different definitions). We remark that the declining tail of f_{ac} towards smaller granules sizes illustrates that employing a logarithmic scale for the histograms of the granule size is essential to yield correct conclusions on the declining distribution of the smallest granules. We find for the so-

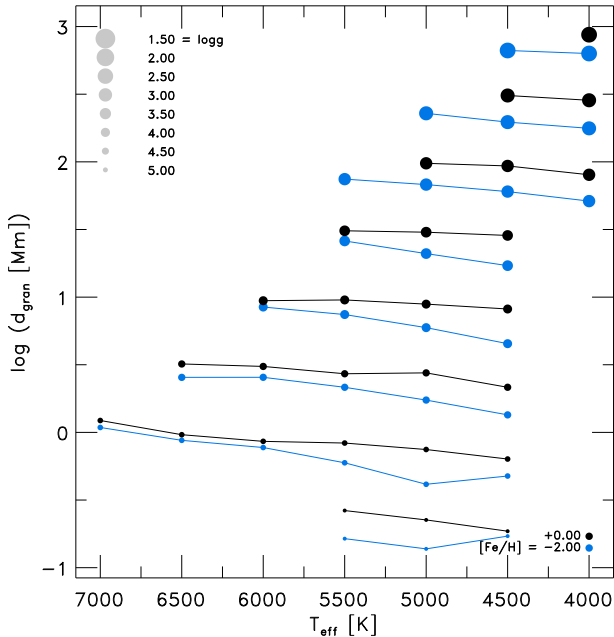


Fig. 4: The mean granule size vs. effective temperature for different stellar parameters.

lar simulation a dominant scale of $A_{ac} = 2.06 \text{ Mm}^2$, which is $d_{ac} = 1.62 \text{ Mm}$. Observational findings have similar values with $d_{ac} \approx 1 \text{ Mm}$ (Roudier & Muller 1986; Hirzberger et al. 1997). The given difference arises probably from atmospheric and instrumental effects (Stein & Nordlund 1998).

In the following, we discuss the resulting granule sizes for different stellar parameters. We show in Fig. 3b the histograms of the granule diameters, d_{gran} . And we show the mean granule size for different stellar parameters in Fig. 4. For higher T_{eff} and $[\text{Fe}/\text{H}]$ the mean granule sizes are slightly larger, while these are significantly larger for giants (lower $\log g$), since the pressure scale height scales with the surface gravity (see Paper I). In general, the shapes of the histogram are similar to the solar one and also exhibit a distinct maximum in their granule sizes. In the case of dwarfs, the peak of d_h is less pronounced towards lower T_{eff} and we find increasingly a bimodal distribution in the histograms of the granule diameter with a distinct second peak from the small-scale granules, in particular, for cooler models (Fig. 3b). The second peak at smaller granule sizes varies with stellar parameter, so that in some cases the two peaks are reversed. In these models the granules fragment into smaller pieces more efficiently (see Sect. 4). However, most of radiation still emerges from the larger peak, since the area contribution function exhibits a single peak, which is located at larger granule size (see Fig. 3b, where we have marked d_{ac}). Furthermore, the decline towards larger fragmenting granules is steeper with higher T_{eff} , which means that these granules are prone to disintegrate within a smaller range of granule sizes. The lower half of the histograms are similar despite a shift and the second peak.

In Paper I, we estimated the typical granule size from the location of the maximum of the 2D spatial power-spectrum of the intensity, d_{Int} . Furthermore, we found d_{Int} to correlate well with pressure scale height just below the optical surface. In Fig. 5, we compare the mean granule size, d_{gran} , with the estimated granule size from the power-spectrum of the intensity d_{Int} . The two correlate very well for all of our atmosphere models.

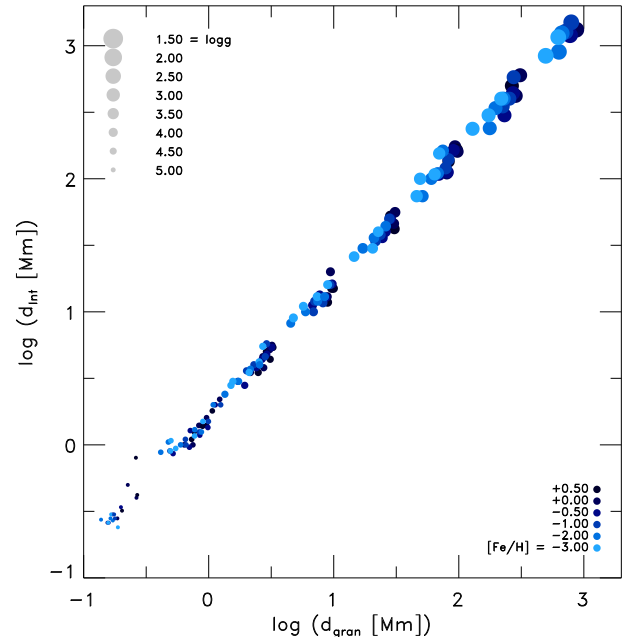


Fig. 5: The length-scale at the maximum of the temporally averaged 2D spatial power-spectrum of the intensity, d_{Int} , vs. the mean granule size, d_{gran} , for different stellar parameters.

Our findings carry some uncertainty that might be rooted in the granule detection method or in the simulation boundaries. However, we have confirmed that our results are robust, since these are qualitatively similar to those by Beeck et al. (2013b). They used also the multiple level tracking algorithm, and found also an asymmetric distribution exhibiting a dominant granule size with an extended tail for the small-scale granules. Moreover, the mean granule diameters and the filling factors they found are similar to our results.

4. Fractal dimension

The fractal dimension is a suitable, measurable value to quantify the complexity of a geometrical shape (Mandelbrot 1977). In the case of granules, this is given by the area-perimeter relation

$$P = kA^{D/2} \quad (3)$$

with k being a shape factor and D the fractal dimension (Roudier & Muller 1986). In planar geometry, ideal objects have an integer fractal dimension, e.g., circles or squares have $D = 1$ (dimension of a line), but with different shape factors $k = 2\sqrt{\pi}$ and 4, respectively. However, real objects are of fractal nature. It is an important measure for the regularity of granules; more regular ones will have a lower D , while more irregular granules will have higher area-perimeter ratios.

We show the 2D histogram of the area and perimeter determined from the granules of the solar simulation in Fig. 6a with a tight correlation. At the dominant granule size, we find a distinct change in the slope of the correlation, indicating a multi-fractal nature of granulation. Therefore, we determined two fractal dimensions with two separate linear least-square fits. The first one is performed for the small-scale granules ($A < \bar{A}$), and the resulting fractal dimension is very close to unity with $D_1 = 1.04$, which means that the smaller granules are regularly shaped. One

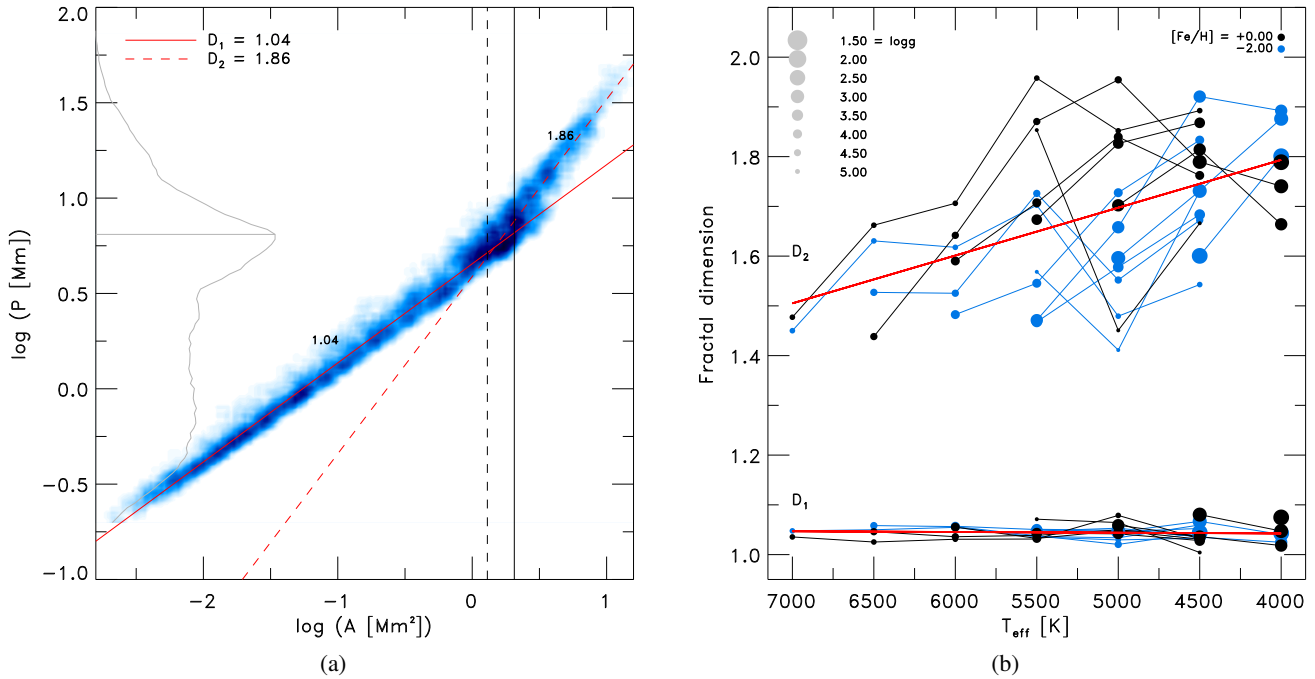


Fig. 6: *Left figure*: We show the (smoothed) histogram of the area-perimeter relation determined from the solar simulation. We indicated the histogram of the perimeter (*gray line*), the location of the mean granule area (*black dashed*) and the maximum of f_{ac} (*black solid line*). Also the linear fit for the small-scale (*red solid*) and the large granules (*red dashed lines*) are also included. *Right figure*: The fractal dimensions, D_1 and D_2 , for different stellar parameter. Furthermore, we included linear fits for D_1 and D_2 , and the slopes are $\Delta_1 \approx 1.06$ and $\Delta_2 \approx 2.18$.

can also consider this in the way that for a granule that is expanding the perimeter is increasing with the square root power of the area (same to a circle), and therefore, these granules will be more regular shaped. The second linear fit is performed for larger granules ($A > \bar{A}$), and the fractal dimension is distinctively larger with $D_2 = 1.86$ (see Fig. 3a). This means that large granules feature increasingly larger perimeters.

The fractal dimension has been determined from solar observations. In agreement with our result, Roudier & Muller (1986) found two distinct fractal dimensions with $D_1 = 1.25$ and $D_2 = 2.15$ with a Fourier-based recognition (FBR) method. Our fractal dimensions also coincide with Hirzberger et al. (1997), who determined for smaller granules $D_1 \approx 1.3$ and for larger granules $D_2 \approx 2.1$ (with FBR). Bovelet & Wiehr (2001) derived $D_1 = 1.2$ and $D_2 = 1.96$. On the other hand, Bovelet & Wiehr (2001) determined with their multiple layer tracking method distinctively lower values for the fractal dimensions with $D_1 = 1.09$ and $D_2 = 1.28$. Their smaller fractal dimension is similar to ours, however, the second one for the larger granules is much lower. They find that the FBR method is recognizing smaller granules as a larger single one compared to the multiple layer tracking method. However, since we do not use a FBR method, our results should be similar to their findings. We also performed a single linear fit, which resulted in $D = 1.10$, but the latter is clearly insufficient to depict the larger granules (not shown). In many of these cases, the fractal dimensions are slightly larger than our values, which probably originates from the different granule recognition method (FBR), but also from the reduced resolution of their observations that include atmospheric effects.

Figure 6b shows the variation of the area-perimeter ratio based on D_1 and D_2 for different stellar parameters. The branch-

ing at the dominant granule size scale is always given with a slope close to unity for the smaller granules and a steeper slope for larger granules, in particular for lower T_{eff} and higher $[\text{Fe}/\text{H}]$. The fractal dimension for the smaller granules is close to unity with the average value being $D_1 = 1.05 \pm 0.02$, and therefore basically universal for all simulations. This means that granules smaller than the dominant granule size are mostly regularly shaped. Furthermore, a value close to unity implies that the perimeter increases to the square root with the area, i.e. $P \propto A^{1/2}$, for the smaller granules (see Eq. 3). The second dimensions are clearly larger, being on average $D_2 \approx 1.7 \pm 0.3$ with a significant level of scatter due to the stellar parameters, featuring a general decreasing trend for higher T_{eff} and $[\text{Fe}/\text{H}]$, and lower $\log g$. D_2 never exceeds 2 in every of our simulations. The larger granules above the dominant granule size are irregularly shaped, and $D_2 \sim 2$ translates into a linear area-perimeter relation of $P \propto A$. This is in principle the manifestation of the fragmentation of oversized, unstable granules. When we consider a hotter/cooler dwarf ($T_{\text{eff}} = 7000/5500 \text{ K}$, $\log g = 4.5$ in Fig. 6b), then the values for D_2 are ~ 1.5 and ~ 1.9 . If we compare two granules with the same (larger) area, A_0 , from both dwarfs, then the granules of the cooler dwarf will exhibit much larger perimeters, $P_{\text{hot}}(A_0) < P_{\text{cool}}(A_0)$, i.e. its granules will be in general more fragmented. This might be due to the higher densities and the lower vertical velocities, thereby shifting the balance of the characteristic length scales (see Paper III).

The granulation pattern in our simulations exhibit a striking self-similarity despite the large variations in the horizontal length scales and convective flow properties (see Fig. 1). This observation is backed by the linear correlation of the area-perimeter relations, and the similar fractal dimensions between

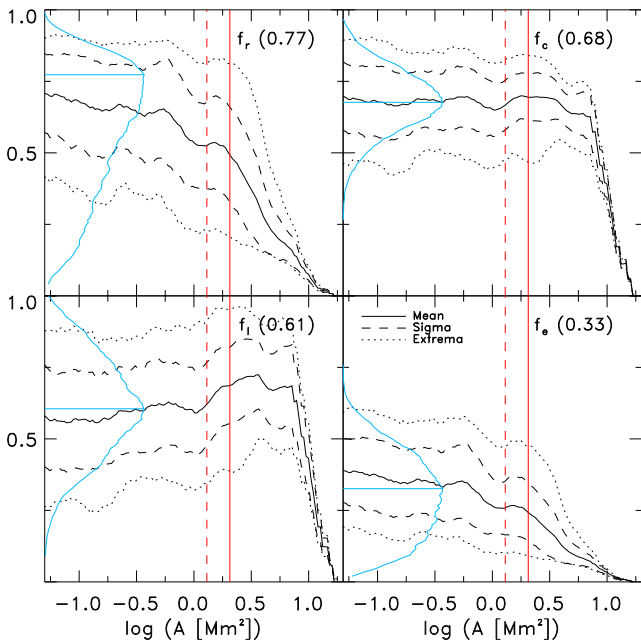


Fig. 7: The smoothed distribution of the geometrical shape factors for roundness, circularity, elongation and ellipticity vs. granule area derived from the solar simulation. We outlined the mean (*solid*), the standard deviation around mean (*dashed*) and the extrema (*dotted lines*). Furthermore, we included also a (smoothed) histogram of the shape factor (*blue lines*), in order to render its distribution. The maximum of the latter is indicated (*horizontal blue line*). The vertical lines indicate mean and dominant granule area (*red vertical dashed and solid line*).

the different stellar parameters. Surface convection appears to operate scale-invariant over large ranges. This is true, in particular, for the small-scale granules. Furthermore, the branching of the two fractal dimensions is taking place at the dominant granule size for all stellar parameters, since above the latter the granules cannot be supported by the pressure excess and start to fragment, thereby increasing the granule perimeter and becoming more irregular. Therefore, the branching area between D_1 and D_2 can be regarded as the maximal granule size, with granules of larger sizes being unstable.

5. Geometrical properties

To quantify the geometrical properties of the complex granule shapes, we followed Hirzberger (2002) and determined

$$f_r = 4\pi A/P^2, \quad (4)$$

$$f_c = d_{\text{gran}}/d_{\text{MF}}, \quad (5)$$

$$f_l = w_{\text{MF}}/d_{\text{MF}}, \quad (6)$$

$$f_e = b/a. \quad (7)$$

The roundness factor (Eq. 4) is the area-perimeter relation that measures the deviation from a perfect circle, and is also known as the isoperimetric quotient. The isoperimetric inequality, $f_s \leq 1$, holds for any arbitrary shape, and yields equality only for the circle. The circularity factor (Eq. 5) is the ratio between granule size, d_{gran} , and the maximal Feret-diameter, d_{MF} , which is the diameter of the principal axis, i.e. the maximum diameter at the barycenter for all degrees of rotation. It quantifies the evenness

along the boundary, where only an even shape will lead to a value close to 1. The elongation factor (Eq. 6) is determined with w_{MF} being the width perpendicular to d_{MF} , i.e. it is the aspect ratio of the principal axis. Finally, the ellipticity factor (Eq. 7) is obtained by $a = \xi + (\xi^2 - A/\pi)^{1/2}$ and $b = A/(\pi a)$ with $\xi = [(A/\pi)^{1/2} + P/\pi]/3$, and compares the shape with an ellipse (see Hirzberger 2002).

The geometrical properties are shown for the Sun in Fig. 7. For granules smaller than the dominant granule size, the geometrical properties are in general very similar. Above d_{ac} one finds a transition, in particular, f_r and f_e are dropping towards zero above the dominant granule size, since the granules start to fragment and split, and the perimeter is increasing much faster than the area ($f_r \propto P^{-2}$). This is in agreement with the second, larger fractal dimension, D_2 , discussed in Sect. 4. The shape factors f_c and f_l are independent of the perimeter. The histograms of the shape factors are symmetrically distributed around a well-defined maximum with different widths. However, the roundness factor is an exception, it exhibits a skewed distribution that covers almost the whole range between zero and unity, and the maximum is located at $f_r = 0.77$. As given in Fig. 7, the contributions arise from different granules sizes. Smaller granules tend to be in general more regular at their boundaries (larger f_r) with smooth edges, while the fragmenting granules that are larger than d_{ac} have increasingly irregular, complex boundaries (small f_r) that are fringed and convoluted (see Fig. 1). The granule shapes are in overall regular, circular shapes ($f_c = 0.68$ and $f_l = 0.61$) independently from d_{gran} . Furthermore, the granules are quite elongated with $f_e = 0.33$. When we compare our four shape factors with those by Hirzberger (2002), then these are qualitatively very similar, only the maximum of the roundness factor is at much lower values with $f_r = 0.1$, which might be due to differences in the recognition methods. Therefore, we remark that our solar simulation harbors a realistic granulation pattern. Since the shape factors are very similar for different stellar parameters, we restrict ourselves to the discussion of the solar values only.

6. Properties with granule size

6.1. Intensity distribution of granules

In Fig. 8a, we show the mean (bolometric) intensities of granules (seen at the disk-center), $\langle I_g \rangle$, that are normalized by the temporal average of the entire simulation, $\langle I \rangle$, against their granule sizes. Smaller granules are darker (5–9%) and larger granules are brighter. Around the dominant granule size, d_{ac} , one finds the brightest granules (5–15%). This means that the most abundant granules with sizes similar to d_{ac} cover most of the stellar surface and are the brightest, i.e. these dominate the bolometric intensity not only due to their size and abundance, but also brightness. Therefore, most of the radiative energy is lost in these granules. The mean intensities of granules larger than d_{ac} are lower than the maximal, since these large fragmenting (exploding) granules develop dark spots due to pressure excess and mass flux reversal (see Stein & Nordlund 1998), which is then reducing the mean intensity. Hirzberger et al. (1997) finds also a similar granule size dependence for the mean intensity in the observed solar granules.

For higher T_{eff} , smaller granules are dimmer and the larger ones are brighter, while for different $\log g$ the changes are only subtle. In the case of metal-poor simulations, the same small-scale granules are darker for hotter T_{eff} and brighter for cooler T_{eff} compared to the solar case, which correlates with the enhancement of the intensity contrast at lower metallicity (see Pa-

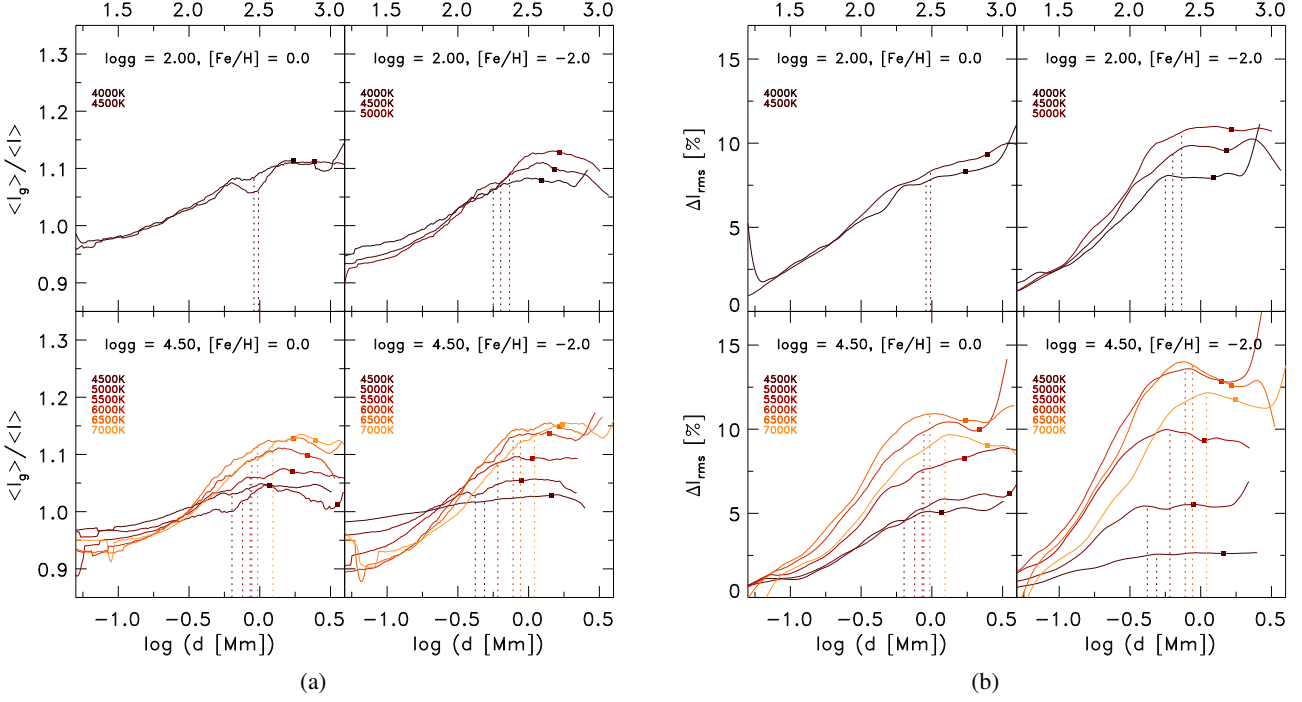


Fig. 8: *Left figure*: Mean normalized intensity vs. granule size. Furthermore, we indicated the mean granule diameters (*dotted lines*) and the dominant scales, d_{ac} (*filled squares*). Note the difference in abscissa between the top and bottom panel. *Right figure*: Mean intensity contrast vs. granule size. Furthermore, we indicated the dominant scales, d_{ac} (*filled squares*). Note the difference in abscissa between the top and bottom panel.

per I). Due to the lack of metals at lower metallicity, the importance of neutral hydrogen as primary electron-donors increases for higher T_{eff} , and since the electron density is controlling the formation of negative hydrogen – the dominant opacity source – the opacity is therefore more sensitive to an increase in temperature.

The intensity contrast of the granules vs. their size is shown in Fig. 8b. The trends are similar to the intensity with stellar parameters. The intensity contrast is lower for small granules, typically reach a maximum at the mean granule size, and decreasing above it. Higher intensity contrast correlates with more complex substructures in the granules with dark spots and bright edges. These arise due to differences in the temperature excess of the granules originating from the granular dynamics (e.g., Hirzberger et al. 1997; Stein & Nordlund 1998).

6.2. Temperature and density of granules

We averaged the temperatures and densities of the recognized granules (Sect. 2) on layers of constant Rosseland optical depth at the optical surface ($\tau_{\text{Ross}} = 1$). In Fig. 9 we show the temperatures against the granule sizes for different stellar parameters. Since the densities are essentially the same as the temperatures, we refrain from showing them. To improve the comparison the displayed mean values of the granules, $\langle T_g \rangle$ and $\langle \rho_g \rangle$, are normalized to the temporal and horizontal averages, $\langle T \rangle$ and $\langle \rho \rangle$, at the surface ($\tau_{\text{Ross}} = 1$) of the whole simulation. In general, larger granules feature higher mean temperatures and lower densities. An inverse correlation between the temperature and density is to be expected (from ideal gas law follows $T \sim p/\rho$). The temperature excess peaks around the mean granule diameters (1–4%), while these are the most under-dense granules at the same time

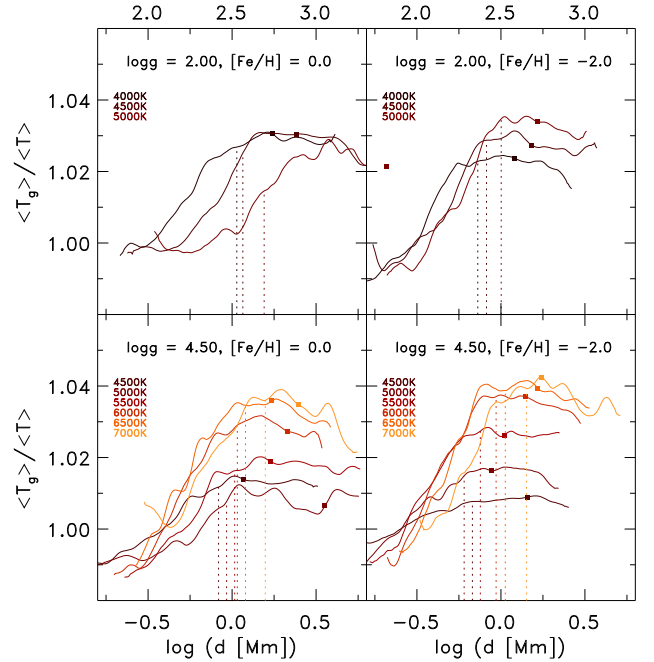


Fig. 9: Mean normalized granule temperature vs. granule size, which is obtained on layers of constant Rosseland optical depth. Furthermore, we indicated the mean granule diameters (*dotted lines*) and the dominant scales, d_{ac} (*filled squares*). Note the difference in abscissa between the top and bottom panel.

(1–15%). The T -peak and ρ -minimum are increasing for higher T_{eff} and lower $\log g$. The smallest granules exhibit lower-than-

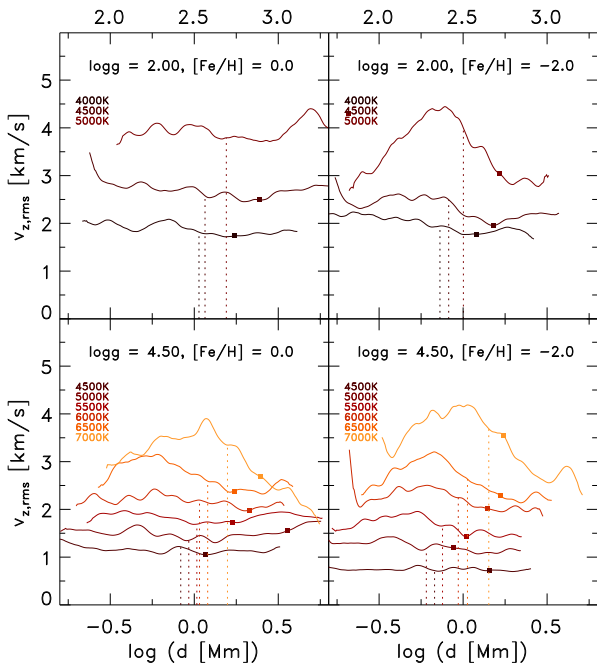


Fig. 10: Mean rms vertical velocity of granules vs. granule size, which is obtained on layers of constant Rosseland optical depth. Furthermore, we indicated the mean granule diameters (*dotted lines*) and the dominant scales, d_{ac} (*filled squares*). Note the difference in abscissa between the top and bottom panel.

average temperatures and higher-than-average densities, since these are small granule fragments located in the downdrafts. Furthermore, we find a tight correlation between the mean granule temperature and intensity with typical values around $\sim 97\%$ with very small variation of different stellar parameters, while the density is anti-correlated with the intensity by values around $\sim -55\%$, but with a large variation with stellar parameters. We note that the normalized mean thermodynamic pressure of granules, $\langle p_{th} \rangle$, exhibits very similar dependence with the granule size as the density, while the mean entropy resembles the temperature, but on a smaller scale (not shown).

6.3. Velocity of granules

In Fig. 10, we show the mean rms of the vertical velocity derived for the individual granules on layers of constant Rosseland optical depth at the optical surface. The rms velocity are increasing for higher T_{eff} , lower $\log g$ and higher $[Fe/H]$. These are in general flat for lower T_{eff} , while for higher T_{eff} , one can find a distinct peak close to the mean granule diameter. We have seen above (Sect. 6.2) that these granules with mean diameters have lower densities due to higher temperatures, therefore, these lighter granules will experience a larger buoyancy acceleration. We remark that the characteristic variations of the rms velocities arise mainly from the upflowing material. We find that the lower mean densities around the mean granule diameters are not decreasing the mean upwards directed vertical mass flux, since the higher velocities are raising the upwards mass transport.

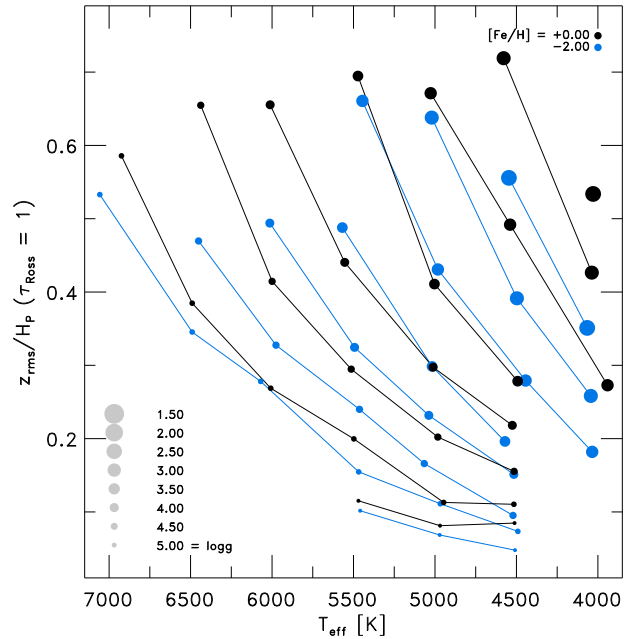


Fig. 11: Overview of the rms deviation of the geometrical depth for optical depth unity that is normalized with the pressure scale height for different stellar parameters.

7. The optical surface

7.1. Corrugation of the optical surface

The optical surface is defined as the layer with optical depth unity ($\tau_{Ross} = 1$), and marks the photospheric transition boundary to the outside. The optical surface is corrugated depending on whether one is considering a region above a granule or one above the intergranular lane, since the local optical depth depends primarily on the integral of the temperature and its gradient. Therefore, we observe the emitted light above granules from higher layers, while the radiation from the intergranular lanes originates from slightly deeper geometrical layers. In Fig. 12, we show the optical surfaces for four different stellar parameters, encompassing the Sun, a turnoff star, a K-giant and a K-dwarf. Furthermore, we also illustrate the vertical velocity at the optical surfaces, showing that the downflows are located in the intergranular lanes, while the granules are flowing upwards at the surface.

The level of corrugation differs for the different stellar parameters. The level of corrugation can be quantified with the temporal averaged rms deviation of the geometrical depth for the layers of constant optical depth unity, i.e. $\langle z_{rms}(\tau_{Ross} = 1) \rangle$. The solar simulation is slightly corrugated with ~ 33 km, which is close to the value found by Stein & Nordlund (1998) with ~ 30 km. Compared to the solar radius this is a very small relative variation: $\sim 5 \times 10^{-3} \%$. In comparison the Earth surface has a tolerance of 0.17% from a spheroid, which is ~ 30 times larger than the (quiet) Sun. The turnoff and giant simulation exhibit much larger corrugated optical surfaces compared to the Sun with 300 and 23 000 km respectively, while the dwarf model has a very smooth optical surface with 3 km. One can estimate that the turnoff star has approximately twice the solar radius, while the K-giant is twenty times higher, making the relative variations 0.02 and 0.17%, respectively. The K-dwarf would

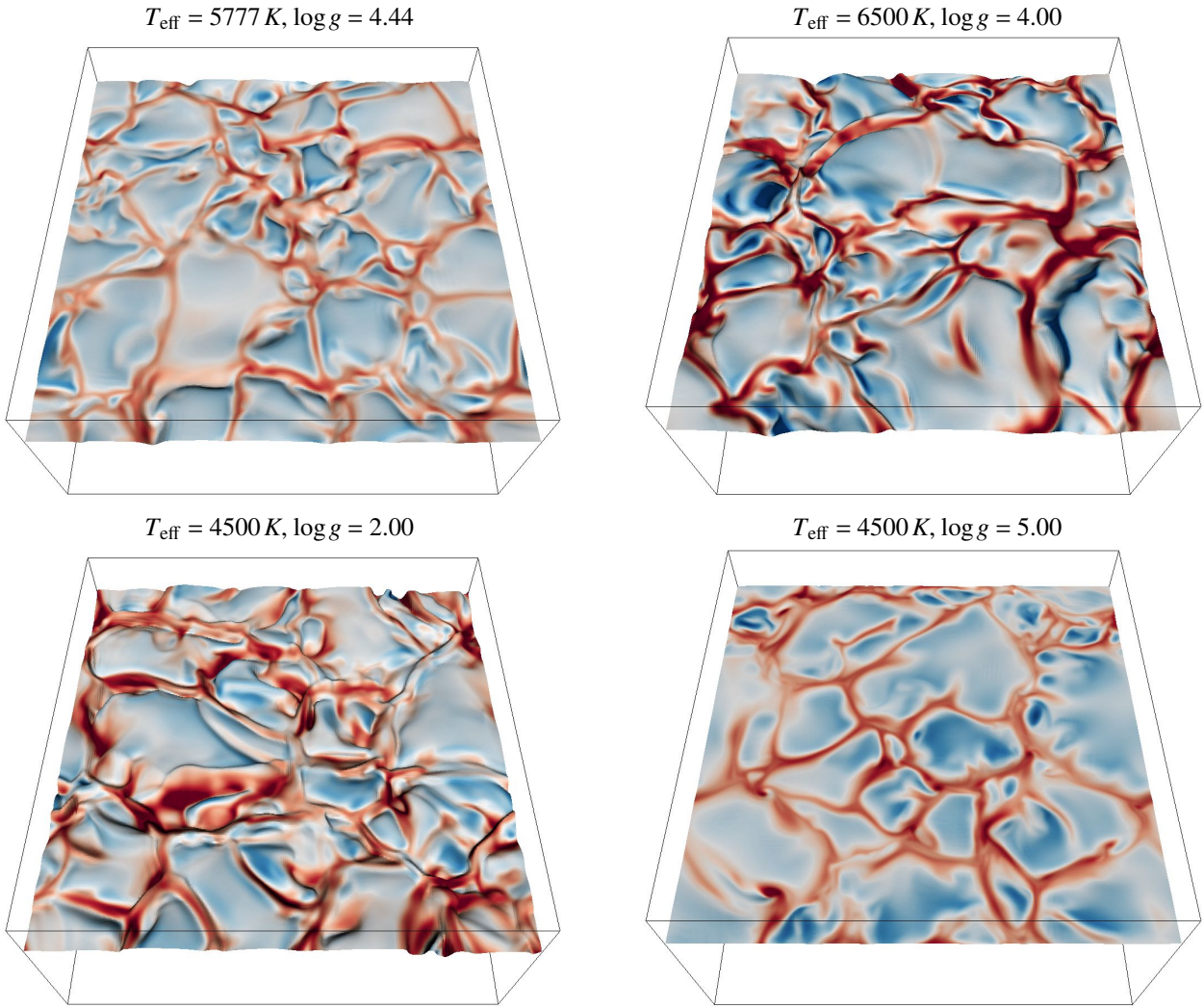


Fig. 12: The corrugated optical surface with the viewing angle $\mu = 0.6$, including the vertical velocity to illustrate the up- and downflows (*blue* and *red*; each with a range of 8 km/s) for a selection of stars: Sun (5777 K/4.44), turnoff (6500 K/4.0), K-giant, K-dwarf with solar metallicity.

have half of the solar radius and a very small relative variation with $\sim 1 \times 10^{-3} \%$.

To illustrate the systematic variation of the corrugation, we overview the standard deviation of $\langle z(\tau_{\text{Ross}} = 1) \rangle$, which is normalized by the (total) pressure scale height in Fig. 11. The corrugation increases primarily with lower surface gravity and higher effective temperatures, since from hydrostatic equilibrium ($dp/dz = \rho g$) follows $dz \propto 1/g$ and the dominant negative hydrogen opacity source is very temperature sensitive ($\kappa_{\text{H}^-} \propto T^{10}$; Stein & Nordlund 1998). Furthermore, at higher metallicity the corrugations are also larger due to the lower densities.

7.2. Surface velocity correlations

In order to study the surface properties more closely, we determined the temporally averaged (2D) histograms for the temperature, T , density, ρ , and intensity fluctuations, δI , as a function of vertical velocity at the optical surface on layers of geometrical depth ($\langle \tau_{\text{Ross}} \rangle = 1$) or constant Rosseland optical depth ($\tau_{\text{Ross}} = 1$), as shown in Fig. 13. The thermodynamic properties correlate very well with vertical velocity, and the vertical velocity is separating the different properties between the up-

and downflows (see SN98). All the thermodynamic properties exhibit a bimodal distribution due to the inherent asymmetric nature of the convective energy transport. On the one hand, the stellar plasma in the upflows has hotter temperatures and lower densities with brighter intensities located in the granules. On the other hand, the downflows are composed by cooler temperatures and higher densities with darker intensities found in the intergranular lane. Furthermore, the (slower) upflows correlate with higher entropy and ionization, while the (faster) downflows associate with lower entropy and ionization. In Fig. 13 we show the mean values of the histograms for T , ρ and δI , which exhibits typically a s-shape. Moreover, we display the contours of one-fifth of the maximal probability for the T and ρ . Then one can obtain a temperature jump from the histograms derived on layers of constant geometrical depth (left panel in Fig. 13), where we determined the height of the optical surface on the temporal average, i.e. $\langle \tau_{\text{Ross}} \rangle = 1$. At a higher effective temperature the density decreases, while the velocity rises, thereby leading to an enhancement in the overshooting of the convective upflows, which is also known as "naked granulation" (Nordlund & Dravins 1990). In agreement with the latter, we find that the T -jump becomes more distinct for hotter T_{eff} , and the bi-

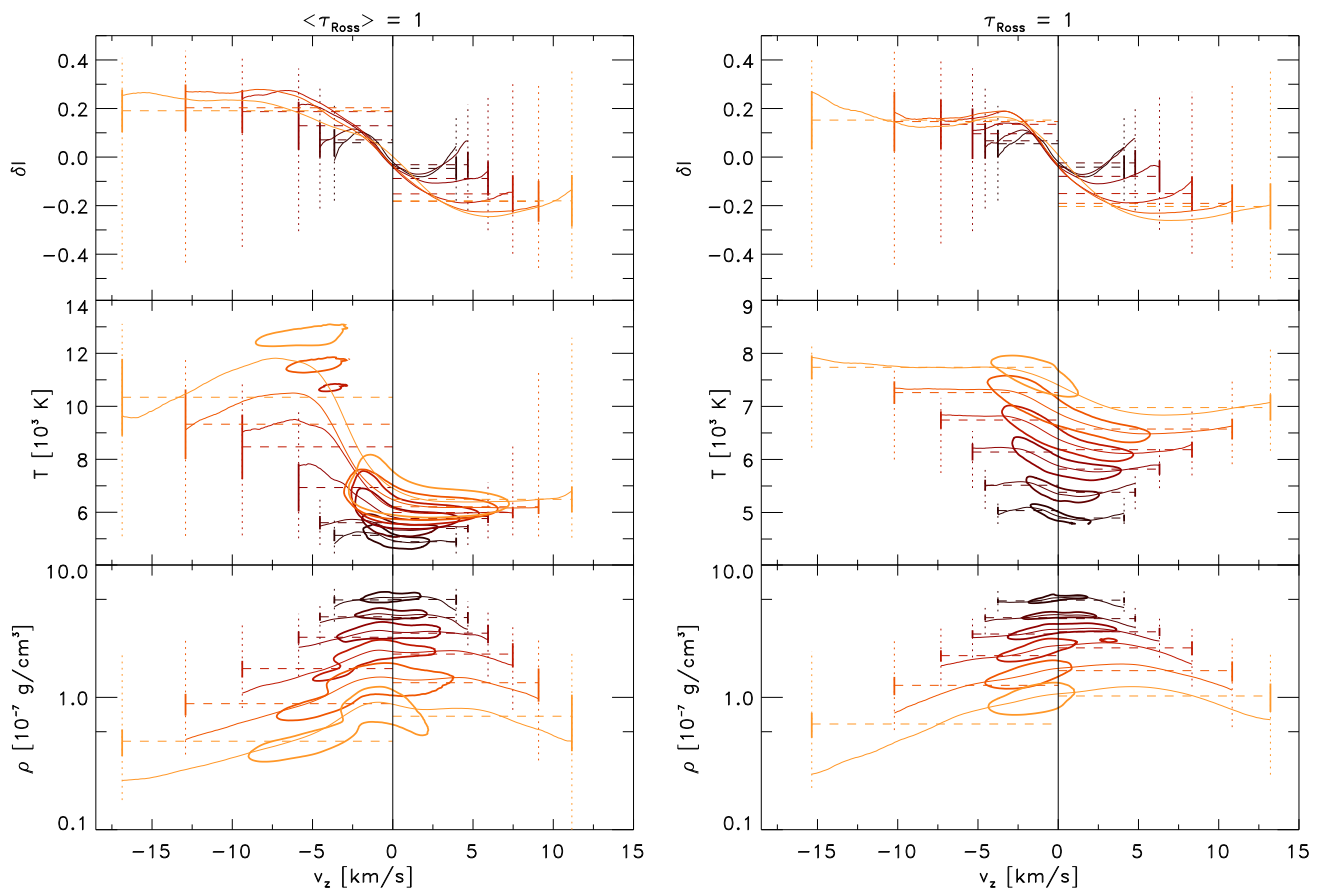


Fig. 13: Correlation of the relative intensity fluctuations, temperatures, and densities with the vertical velocities at the optical surface for different stellar parameters (top, middle and bottom panel respectively) shown by the distribution of their histogram (normalized histogram at 0.2 is shown with thick contour lines). We indicated the mean value (solid line), and for the up- and downflow separately their mean (horizontal dashed line), range (vertical dotted line) and standard deviation (vertical solid line). Furthermore, we show the geometrical averages taken at the height with $\langle \tau_{\text{Ross}} \rangle = 1$ (left panel) and the averages on layers of constant optical depth $\tau_{\text{Ross}} = 1$ (right panel).

modal distribution between the up- and downflows is more evident (compare the mean values between the up- and downflows). The upflows have distinctively larger values compared to averages on layers of constant optical depth (right panel in Fig. 13). The velocity correlation is tighter at layers of constant optical depth ($\tau_{\text{Ross}} = 1$), since the opacity is very T -sensitive due to the negative hydrogen opacity, and layers with similar temperatures are mapped during transformation to the optical depth (see Paper II). The fluctuations of the upflows are broader in temperature and narrower for the density (see Fig. 13), while the downflows feature a broad distribution in ρ and smaller ranges in T .

8. Conclusions

We derived extensive details of stellar granulation by applying the multiple layer tracking algorithm for the detection of granules imprinted in the emergent (bolometric) intensity map, which was originally developed for solar observations. This method works very reliable for different stellar parameters. Then, we determined for the individual detected granules properties: diameter, intensity, temperature, density, velocity and geometry. The granule diameters span a large range, therefore, we advise the use of a logarithmic equidistant histogram, since otherwise, the smaller scales are under-resolved, which leads to the misinterpretation of a large population of small granules. A distin-

guished dominant granule size can always be determined with the maximum of the area contribution function, which is often very close the maximum of the diameter distribution. Furthermore, we find two distinct fractal dimensions (slopes of the area-perimeter relation) that are divided at the dominant granule size. For smaller granules the fractal dimension is always very close to unity, which points out that these are evenly shaped. The larger granules have distinctively larger fractal dimensions close to 2, primarily depending on the effective temperature. For lower T_{eff} we find fractal dimension being larger. In the case of the solar simulation, the dual fractal dimensions we find is in contradiction to the finding by Bovelet & Wiehr (2001), who finds only a single fractal dimension with the same method from solar observations, and the discrepancy might root in observational constraints. The bifurcation of the fractal dimension above the dominant granule size arises simply due to the fragmentation of granules, which will inevitably entail that the perimeter increases. We studied also the properties prevailing at the optical surface in our stellar atmosphere simulations. We find that the corrugation of the optical surface increases for higher T_{eff} and lower $\log g$. Also, we revealed the systematic correlation of the intensity, temperature and density with the vertical velocity as a natural consequence of the convective energy transport.

References

- Abramenko, V., Yurchyshyn, V., Goode, P., & Kilcik, A. 2010, *ApJ*, 725, L101
- Abramenko, V. I. & Longcope, D. W. 2005, *ApJ*, 619, 1160
- Abramenko, V. I., Yurchyshyn, V. B., Goode, P. R., Kitiashvili, I. N., & Kosovichev, A. G. 2012, *ApJ*, 756, L27
- Asplund, M., Grevesse, N., Sauval, A. J., Allende Prieto, C., & Kiselman, D. 2004, *A&A*, 417, 751
- Asplund, M., Nordlund, Å., Trampedach, R., Allende Prieto, C., & Stein, R. F. 2000, *A&A*, 359, 729
- Beeck, B., Cameron, R. H., Reiners, A., & Schüssler, M. 2013a, *A&A*, 558, A48
- Beeck, B., Cameron, R. H., Reiners, A., & Schüssler, M. 2013b, *A&A*, 558, A49
- Bovelet, B. & Wiehr, E. 2001, *Sol. Phys.*, 201, 13
- Bovelet, B. & Wiehr, E. 2007, *Sol. Phys.*, 243, 121
- Carlsson, M., Stein, R. F., Nordlund, Å., & Scharmer, G. B. 2004, *ApJ*, 610, L137
- Chiavassa, A., Bigot, L., Kervella, P., et al. 2012, *A&A*, 540, A5
- Chiavassa, A., Haubois, X., Young, J. S., et al. 2010, *A&A*, 515, A12
- Chiavassa, A., Pasquato, E., Jorissen, A., et al. 2011, *A&A*, 528, A120
- Chiavassa, A., Plez, B., Josselin, E., & Freytag, B. 2009, *A&A*, 506, 1351
- Collet, R., Asplund, M., & Trampedach, R. 2006, *ApJ*, 644, L121
- Collet, R., Asplund, M., & Trampedach, R. 2007, *A&A*, 469, 687
- Freytag, B., Steffen, M., Ludwig, H.-G., et al. 2012, *Journal of Computational Physics*, 231, 919
- Hirzberger, J. 2002, *A&A*, 392, 1105
- Hirzberger, J., Bonet, J. A., Vázquez, M., & Hanslmeier, A. 1999a, *ApJ*, 515, 441
- Hirzberger, J., Bonet, J. A., Vázquez, M., & Hanslmeier, A. 1999b, *ApJ*, 527, 405
- Hirzberger, J., Vazquez, M., Bonet, J. A., Hanslmeier, A., & Sobotka, M. 1997, *ApJ*, 480, 406
- Janßen, K., Vögler, A., & Kneer, F. 2003, *A&A*, 409, 1127
- Kučinskas, A., Steffen, M., Ludwig, H.-G., et al. 2013, *A&A*, 549, A14
- Ludwig, H.-G., Caffau, E., Steffen, M., et al. 2009, *Mem. Soc. Astron. Italiana*, 80, 711
- Magic, Z., Chiavassa, A., Collet, R., & Asplund, M. 2014a, *ArXiv e-prints*
- Magic, Z., Collet, R., Asplund, M., et al. 2013a, *A&A*, 557, A26
- Magic, Z., Collet, R., Hayek, W., & Asplund, M. 2013b, *A&A*, 560, A8
- Magic, Z., Weiss, A., & Asplund, M. 2014b, *ArXiv e-prints*
- Mandelbrot, B. B. 1977, *The fractal geometry of nature*
- Nordlund, A. 1982, *A&A*, 107, 1
- Nordlund, A. & Dravins, D. 1990, *A&A*, 228, 155
- Nordlund, Å., Stein, R. F., & Asplund, M. 2009, *Living Reviews in Solar Physics*, 6, 2
- Pereira, T. M. D., Asplund, M., Collet, R., et al. 2013, *A&A*, 554, A118
- Pereira, T. M. D., Asplund, M., & Kiselman, D. 2009a, *A&A*, 508, 1403
- Pereira, T. M. D., Kiselman, D., & Asplund, M. 2009b, *A&A*, 507, 417
- Ramírez, I., Allende Prieto, C., Koesterke, L., Lambert, D. L., & Asplund, M. 2009, *A&A*, 501, 1087
- Ramírez, I., Allende Prieto, C., & Lambert, D. L. 2008, *A&A*, 492, 841
- Ramírez, I., Collet, R., Lambert, D. L., Allende Prieto, C., & Asplund, M. 2010, *ApJ*, 725, L223
- Roudier, T. & Muller, R. 1986, *Sol. Phys.*, 107, 11
- Schrijver, C. J., Hagenaar, H. J., & Title, A. M. 1997, *ApJ*, 475, 328
- Solanki, S. K. 1993, *Space Sci. Rev.*, 63, 1
- Steffen, M., Ludwig, H.-G., & Kruss, A. 1989, *A&A*, 213, 371
- Stein, R. F. & Nordlund, A. 1998, *ApJ*, 499, 914
- Stein, R. F. & Nordlund, Å. 2006, *ApJ*, 642, 1246
- Trampedach, R., Asplund, M., Collet, R., Nordlund, Å., & Stein, R. F. 2013, *ApJ*, 769, 18
- Tremblay, P.-E., Ludwig, H.-G., Freytag, B., Steffen, M., & Caffau, E. 2013, *A&A*, 557, A7
- Vögler, A. & Schüssler, M. 2003, *Astronomische Nachrichten*, 324, 399
- Wiehr, E. & Bovelet, B. 2009, *Central European Astrophysical Bulletin*, 33, 19